DATA-DRIVEN RECONSTRUCTION AND ENCODING OF SPARSE STIMULI ACROSS CONVERGENT SENSORY LAYERS FROM DOWNSTREAM NEURONAL NETWORK DYNAMICS*

VICTOR J. BARRANCA†, YOLANDA HU†, ZOE POTERFIELD†, SAMUEL ROTHSTEIN†, AND ALEX XUAN†

Abstract. Neuronal networks vary dramatically in size, connectivity structure, and functionality across downstream layers of the brain. This raises the question of whether information is lost as it is re-encoded along compressive and expansive pathways. In this work, we develop a potential *data-driven* mechanism for the preservation of information in the activity of neuronal networks across downstream layers, which uses the widespread linearity of individual neuronal responses to sufficiently strong ramped artificial inputs to fit a linear input-output mapping across the network. We analyze the dynamics of several families of two-layer neuronal network models, where the input components far outnumber the downstream neurons as in compressive pathways, and apply the fitted mapping in conjunction with compressive sensing theory to reconstruct stimuli with sparse structure. The input-output mapping facilitates stimulus reconstructions that only use measurements of downstream neuronal firing rates in response to inputs over a short time duration, furnishing stimulus recovery even when theoretical analysis is intractable or the governing equations of the dynamical system are unknown as in experiment. Similarly accurate stimulus reconstructions are obtained across different single-neuron models, network coupling functions, and image classes. Improved reconstructions are yielded when uniformly-random feedforward connectivity is replaced by spatially localized feedforward connectivity akin to receptive fields. We expect similar principles could be leveraged experimentally in prosthetics as well as in the reconstruction of large-scale network connectivity.

Key words. Neuronal network dynamics, Signal processing, Input-output mappings

AMS subject classifications. 92C42, 92C05, 37N25, 94A08

1. Introduction.

As stimuli are processed in sensory systems, information is encoded in the dynamics of neuronal networks of disparate sizes and connectivity structures. Across downstream layers in the brain, an especially common feature in feedforward connectivity is compression and subsequent re-expansion. In the early human visual system, for example, compression occurs when a stimulus injected into a network of approximately 150 million photoreceptors is subsequently processed by only roughly 1.5 million retinal ganglion cells. Further downstream, information encoded by the millions of neurons in the Lateral Geniculate Nucleus (LGN) is later expanded when re-encoded by the primary visual cortex, which contains approximately 40 times as many neurons as the LGN [10, 103]. Similarly, the human olfactory system begins with about 15 million olfactory receptor neurons that feed into just thousands of glomeruli before re-expansion into a network of millions of neurons in the piriform cortex [121, 118, 92, 86, 102]. This structure has been observed in various auditory and somatosensory systems as well [105, 75, 80, 26], and is therefore hypothesized to be central to efficient coding in the brain [9, 8, 68].

Numerous functional benefits to compression and re-expansion have been proposed and verified theoretically [56, 4]. In the resultant low-dimensional space after compression, neuronal networks have the potential to perform redundancy reduction, prune extraneous sensory data, and facilite especially rapid information processing

*Submitted to the editors DATE.

Funding: This work was supported by NSF grant DMS-1812478 and a Swarthmore Faculty Research Support Grant.

†Department of Mathematics and Statistics, Swarthmore College, Swarthmore, PA (vbarran1@swarthmore.edu, http://www.swarthmore.edu/NatSci/vbarran1/).

This manuscript is for review purposes only.

[71, 124]. Compression onto smaller neuronal networks via parallel pooling may also enhance robustness to noise and improve performance in learning as well as classification tasks [22, 84, 38, 41]. Nonetheless, if not performed intelligently, such massive compression could result in destructive information loss. What potential mechanisms may preserve information across sensory bottlenecks and how are stimuli embedded in the dynamics of low-dimensional neuronal networks?

Previous work has largely investigated this question in the context of learned stimulus representations or highly idealized neuronal network models. Through unsupervised learning, for instance, sparse representations of sets of sub-sampled stimuli can be developed without knowing the sampling structure or sparse basis for the stimuli, but such a framework does not fully address how reconstructions may be obtained without learning or in the context of realistic neuronal network activity [40]. Other approaches leverage linear or discrete-time dynamics to encode sparse sequences of information in the network dynamics, but they do not address the more realistic case of continuous and nonlinear network dynamics [55]. Recent work in the context of simple spiking neuronal network models with nonlinear dynamics has successfully reconstructed natural scenes using measurements of evoked firing rates; however, this line of research requires knowledge of the underlying dynamical equations governing the network activity for a successful reconstruction, which is likely not available to neurons in the brain or in experiments [17, 16, 21].

In this work, we investigate the reconstruction and encoding of stimuli from evoked nonlinear neuronal network dynamics *without* knowledge of the underlying governing equations. We develop a new *data-driven* framework for the recovery of realistic inputs into two-layer neuronal network models by leveraging the ubiquitous linearity of neuronal responses to sufficiently strong stimuli [117, 96, 81]. Using the evoked downstream neuronal activity across the network for a small set of ramped artificial inputs, we first construct an approximate linear input-output mapping intrinsic to the nonlinear network dynamics. With the resultant highly underdetermined linear system reflecting a sensory bottleneck, we use the widespread sparsity of natural stimuli in combination with compressive sensing (CS) theory to reconstruct novel gray-scale natural scene inputs from the evoked downstream neuronal dynamics and thereby gauge the accuracy of input encoding [52, 36]. When using sufficiently unstructured measurements of sparse signals, CS theory facilitates successful reconstructions with a dramatic reduction in sampling rate as compared to classical uniform sampling [100], potentially enabling the preservation of stimulus information across convergent network layers.

We show that this encoding and reconstruction framework is successful for a host of models with varying levels of biological realism, including both current-based and conductance-based integrate-and-fire (I&F) single neuron models [31, 101, 77, 37] and networks with either pulse-coupling or alpha-function coupling between downstream neurons [91, 69, 33, 43]. For alternative inputs, such as Poisson spike train inputs with image-based drive strengths and color image inputs, we also produce successful reconstructions based on the evoked network dynamics. When the uniformly random feedforward connectivity is adapted to reflect the spatial localization common in visual receptive fields, our framework yields improved stimulus reconstructions as expected from the evolutionary selection of sensory system structure.

This work provides a possible mechanism for information preservation across the common compressive and expansive pathways in the brain, which is robust to different modeling choices and is fundamentally consistent with many key physiological observations. Regardless of whether this particular mechanism is utilized by the brain, we

nevertheless provide a proof of concept for the retention of signals across neuronal networks of widely varying sizes. It also lays a possible groundwork for important extensions to large-scale network connectivity reconstructions and improved design of sensory prosthetic devices.

The remainder of the paper is structured as follows. In Sect. 2, we introduce the two-layer network model with a downstream compressive layer that we will study throughout this work, beginning in the context of current-based I&F dynamics with pulse-coupling between downstream neurons. We then develop our data-driven network input-output mapping approximation methodology in Sect. 3 and subsequent CS input recovery framework in Sect. 4. To gauge the encoding properties of the network, here we analyze sample stimulus reconstructions as well as study their robustness to limitations in the measurement data and noise. We show how this input encoding mechanism generalizes to alternative stimulus types in Sect. 5 and extends to more detailed neuronal network models in Sect. 6. Finally, we investigate the impact of the feedforward connectivity structure in Sect. 7 and discuss implications as well as natural extensions of this work in Sect. 8.

2. Two-Layer Network Model with Current-Based Integrate-And-Fire Neuronal Dynamics. To investigate information encoding along compressive pathways, we use the framework of a two-layer feedforward network, consisting of a sensory input layer that transmits the incoming stimulus and a downstream output layer that encodes the stimulus through its nonlinear neuronal dynamics. We model compressive encoding across sensory layers of disparate sizes by assuming that the input layer has significantly more components than the output layer, typically differing by a factor of ten throughout this work.

Our initial analysis will assume that the downstream layer is governed by the dynamics of a pulse-coupled integrate-and-fire neuronal network driven by the input layer signal [31, 91, 101, 32, 88]. The I&F model well reproduces experimentally recorded subthreshold membrane potential dynamics and firing statistics, and it possesses the additional benefit of furnishing relatively computationally inexpensive simulations [1, 96, 116, 15]. For concreteness, we will utilize the current-based I&F model in this section and we will later generalize our framework to the conductance-based setting in Sect. 6.1.

The membrane potential dynamics of the i^{th} neuron in the downstream layer are governed by

$$\frac{dv_i}{dt} = -(v_i - V_R) + \sum_{j=1}^{n} F_{ij} p_j + \frac{S}{N_R} \sum_{\substack{k=1 \\ k \neq i}}^{m} R_{ik} \sum_{l} \delta(t - \tau_{kl}), \tag{2.1}$$

evolving from the resting voltage V_R until reaching firing threshold voltage V_T. At this moment, the neuron fires (spikes), and its voltage is immediately reset to V_R. At the time of the l^{th} spike of the k^{th} neuron, τ_{kl}, instantaneous inputs $(S/N_R)\delta(t - \tau_{kl})$ are injected into all post-connected (post-synaptic) neurons in the downstream layer, where $\delta(\cdot)$ is the Dirac delta function, S is the recurrent connection strength, and N_R is the number of recurrent connections. This pulse-coupling reflects the extremely short time scale of each firing event, and in Sect. 6.2 we will consider impact of finite-time interactions between the downstream neurons.

With respect to the network connectivity structure, we assume m and n are the numbers of downstream I&F neurons and input layer components, respectively, with $n \gg m$ to reflect the compressive layer. The feed-forward connection (adjacency)

matrix between the two network layers is $F = (F_{ij})$; we say that the i^{th} neuron in the downstream layer is post-connected to the j^{th} input component if $F_{ij} \neq 0$. For concreteness, we assume here that the input components randomly and sparsely feed into each downstream neuron, such that each possible feedforward connection is equally probable and each realized connection in F has equal strength, f. In Sect. 7, we will examine the impact of alternative and more realistic feedforward connectivity structure. The constant vector $p = (p_1, \ldots, p_n)$ gives the stimulus component strengths transmitted by the upstream layer neurons, which will be generated by the pixels in an n-component gray-scale image. Since photoreceptors in the early visual system, for example, are known to undergo graded potentials with responses indicative of local light intensities, we initially model the feedforward input from the initial layer as fixed in time [108]. Later, in Sect. 5, we will consider the cases of color image inputs and spiking inputs from the upstream layer.

The downstream recurrent connectivity matrix is similarly given by $R = (R_{ij})$. We assume the probability of a connection is low for both connectivity matrices, generating sparse feed-forward and recurrent connections as often found in experiment [87, 57, 62]. For generality, we assume the downstream neurons are connected, but we can also assume that they are uncoupled without impacting our overall analysis by setting $R_{ij} = 0$ for all i, j [15, 11]. While ganglion cells in the retina, for example, are in some studies measured to be disconnected, there are other cases in which connectivity is observed and yet other scenarios where gap junctions are found between neurons [44, 111, 109]. This modeling framework is meant to capture the essence of compressive sensory pathways and potential frameworks for successful data compression in neuronal dynamics rather than reflecting the specifics found in any one sensory system in a particular organism.

Unless specified otherwise, we choose $n = 10000$ input layer neurons, $m = 1000$ downstream neurons, feedforward connection probability $1/m = 0.001$, and the recurrent connection probability 0.05. We also select nondimensional parameters $V_R = 0$, $V_T = 1$, and $t = 1$ to correspond to a time-scale of $20ms$, as typically produced in nondimensionalization [90, 17, 28]. We generally simulate the time evolution of this model over $0 \leq t \leq 10$, which is comparable to typical human reaction times of $200ms$ [2, 3].

3. Data-Driven Network Input-Output Map Fitting. The issues posed by the encoding of input layer stimuli in the dynamics of the neurons in the downstream layer are two-fold. First, since the pathway is compressive, the inverse problem of recovering the large number of input components from measurements of a relatively small number of downstream neurons is highly underdetermined. Second, the downstream neuronal dynamics are nonlinear and vary in time, making the direct application of linear recovery techniques infeasible.

To address this second problem, previous work had considered the limit of a large downstream network size with high neuronal firing rates and small recurrent communication strength, with coarse-graining techniques analogous to kinetic theory in nonequilibrium statistical mechanics yielding an approximate network input-output mapping [110, 34, 18, 12, 11]. In the Appendix, we include a brief derivation of this approximate *theoretical* input-output mapping for the current-based integrate-and-fire neuronal network as well as a comparison with the data-driven mapping discussed in detail throughout the remainder of this section. This theoretical input-output relationship is static in time and linear, relating the downstream neuronal firing rate vector $\mu = (\mu_1, \ldots, u_m)$ measured from simulation to the injected stimulus vector p

via

$$\mu = \frac{Fp}{(V_T - V_R)} - \frac{e_m}{2} + \frac{S}{N_R\,(V_T - V_R)} R\mu, \tag{3.1}$$

where e_m is an m-vector of ones.

However, analytically deriving such a theoretical mapping is not feasible for more detailed neuronal network models and it is not clear how to obtain an input-output mapping when the underlying equations governing the neuronal dynamics are unknown. To deal with these issues, in this work we instead take a data-driven approach in obtaining such an input-output relationship. We inject into the network a small number of artificial random stimuli, $p^{(1)}, \ldots, p^{(r)}$, ramping up the mean strength of each by adjusting the feedforward connectivity scaling constant f. For each input, we record the resultant firing rate vectors, $\mu^{(1)}, \ldots, \mu^{(r)}$, across the downstream neuronal network.

In Fig. 1 (a), we consider the firing rate response for an individual representative downstream neuron in our model across an ensemble of ramped external inputs. We depict the firing rate as a function of the external input scaling strength, which is a multiplicative factor scaling the generated input stimuli. We see that for sufficiently strong stimulation strengths, the firing rate increases in a highly linear fashion. This is also true for each of the other individual downstream neuronal firing rates as well as for the network-averaged firing rate, though the detailed structure of each curve may vary from neuron to neuron. The linearity of neuronal gain curves is well documented in the context of more realistic neuronal models in many dynamical regimes, including the Exponential Integrate-And-Fire and Hodgkin-Huxley models, as well as in the presence of realistic ionic currents [30, 54, 15, 117]. Experimental recordings have similarly exhibited a linear increase in response with scaled external inputs [117, 96, 81]. Overall, the shape of the gain curve here resembles that of Rectified Linear Units (ReLUs), which are especially effective and common in machine learning applications [82]. If additional biological features are included in the single neuron dynamics, such as a refractory period following action potentials [76, 15], a more sigmoidal gain curve may be obtained, which will still generally have an accurate linear approximation for a broad range of stimulus strengths.

While the resultant firing rate response may vary from neuron to neuron, we can approximate a linear input-output mapping for the i^{th} downstream neuron by

$$\mu_i = \alpha_i (Fp)_i + \beta_i, \tag{3.2}$$

where α_i and β_i are constants produced from a least-squares linear fit of form (3.2) to the firing rate responses of the i^{th} neuron, $\mu_i^{(1)}, \ldots, \mu_i^{(r)}$, across the ramped external inputs, $p^{(1)}, \ldots, p^{(r)}$, in the linear regime of the gain curve. An example of this fitted linear mapping for the previously considered sample neuron is given in Fig. 1 (a). Across all individual neurons in the downstream layer, the collection of these linear maps yields the *data-driven network linear input-output relationship*

$$\mu = \alpha \odot (Fp) + \beta, \tag{3.3}$$

where $\odot$ denotes entry-wise vector multiplication, $\alpha = (\alpha_1, \ldots, \alpha_m)$, and $\beta = (\beta_1, \ldots, \beta_m)$. We call α the *slope* coefficients and β the *intercept* coefficients, corresponding to the parameters for the lines fitted to the respective gain curves of the downstream neurons in the linear dynamical regime.

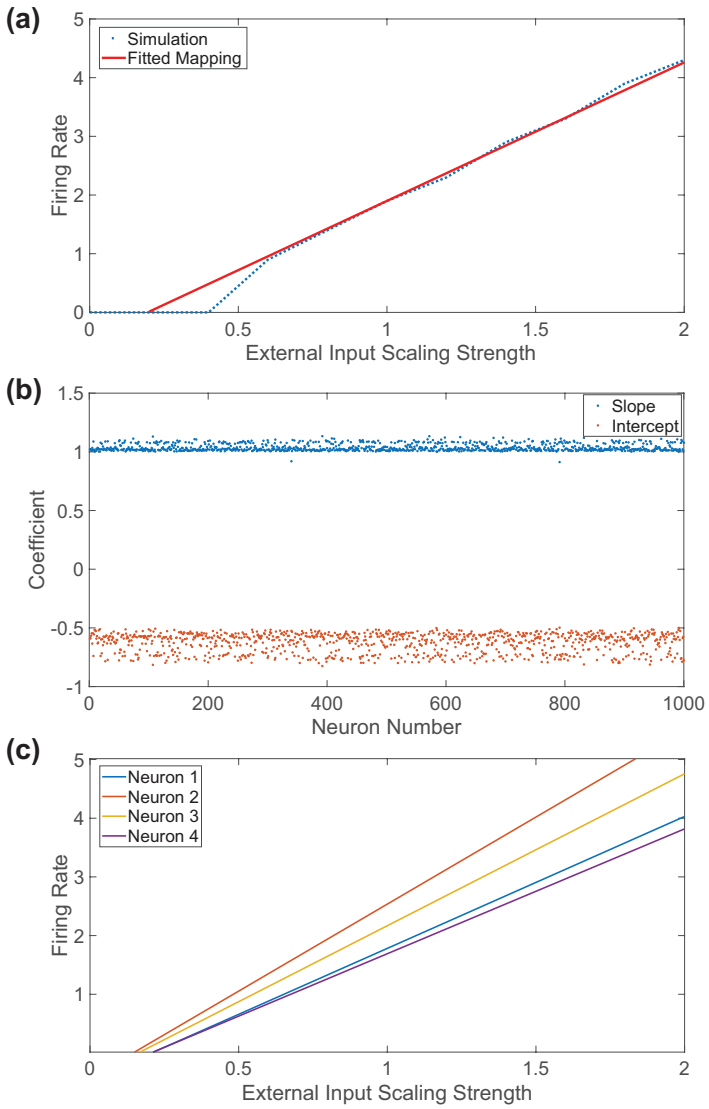


FIG. 1. *(a) Gain curve for an individual representative downstream neuron in the two-layer network with current-based neuronal dynamics prescribed by Eq. (2.1), depicting the individual neuronal firing rate as a function of the external input scaling strength across several simulations with ramped constant external inputs (blue). The input-output mapping for that individual neuron is fitted in the linear regime of the gain curve (red). (b) Slope (blue) and intercept (red) coefficients in the data-driven network input-output mapping given by Eq. (3.3) fitted for each downstream neuron in the two-layer network considered in (a). (c) Fitted linear input-output mappings for several additional sample neurons.*

For this particular idealized two-layer network model, we may validate the data-driven mapping by direct comparison with the known theoretical input-output relationship in Eq. (3.1). The slope and intercept coefficients fitted across the downstream neuronal network are plotted in Fig. 1 (b). Comparing the results obtained from Eq. (3.3) to the theoretical input-output map derived via coarse-graining given by Eq. (3.1), we see close agreement since the α components are clustered around

$\alpha \approx \frac{1}{(V_T - V_R)} = 1$ and the β components are clustered around $\beta \approx -\frac{1}{2}$.

It is important to underline that the data-driven framework for deriving the network input-output map (3.3) does not require knowledge of the governing model dynamical system given by Eq. (2.1). In the particular gain curve considered in Fig. 1, each random vector in the input ensemble is initially generated with mean 2, and to construct different points in the gain curve, each input vector is then multiplied by a distinct external input scaling strength in $[0, 2]$, with 0.2 spacing between scaling strengths. The activity of the downstream neurons in response to each given input vector is recorded over $0 \leq t \leq 10$ to compute the neuronal firing rates used in fitting each individual neuronal input-output mapping. Although there are some minor discrepancies, the linear regime in the gain curve is about the same for all neurons, and using only the random input vectors with mean strength of at least 1 in the fitting process will generally produce an effective network mapping.

As discussed in more detail in the next section, this methodology succeeds with only a small number of ramped input vectors, i.e., 2 or 3 in practice, and for a broad range of external input strengths, so long as these inputs are sufficiently strong such that the firing rate gain is approximately linear. There is generally little variability in the fitted coefficients with the choice of random input vectors utilized. This is to be expected because for a given downstream neuron, the mapping coefficients obtained from different stimulus choices will typically vary no more than the coefficients differ from neuron to neuron across the network as displayed in Fig. 1 (b), since the random differences in the feed-forward connectivity matrix rows mediate random variations in net external input across the downstream neurons. The fitted input-output mappings for several additional downstream neurons are plotted in Fig. 1 (c) for comparison, demonstrating relatively little variability across the network.

We note that it is also possible to fit a linear input-output map that uses data regarding the time-averaged voltages across the downstream layer, $\bar{v}^{(1)}, \ldots, \bar{v}^{(r)}$, corresponding to the respective ramped inputs for models or dynamical regimes in which this data produces a more robust linear mapping of form $\mu = \alpha \odot (Fp) + \beta + \gamma \odot \bar{v}$, with the additional fitted parameter vector γ [20]. For network dynamics governed by Eq. (2.1), however, we have verified that including the voltage term does not alter the encoding capability of the mapping.

4. Stimulus Encoding Across Compressive Layers and Compressive Sensing Reconstructions. In characterizing a potential mechanism through which stimulus information may be successfully encoded in downstream neuronal network dynamics across compressive pathways, we seek to show that it is possible to reconstruct stimulus information from our model network activity. In particular, we aim to use the evoked firing rates of the downstream neurons, given by μ, to recover an input vector with realistic stimulus structure, p, driving the I&F neuronal network dynamics. The error in the resultant reconstruction of the input, p^{recon}, will then be used to assess the accuracy of the stimulus encoding in the downstream layer activity.

With the approximate input-output mapping that is fitted in Eq. (3.3), we have a linear relationship between p and μ. However, to reconstruct p from μ requires solving the related linear system

$$Fp = \frac{1}{\alpha} \odot \mu - \frac{1}{\alpha} \odot \beta \tag{4.1}$$

for unknown vector p, where $\frac{1}{\alpha} = \left(\frac{1}{\alpha_1}, \ldots, \frac{1}{\alpha_m}\right)$. This system is highly underdetermined since the feedforward pathway is compressive and thus $m \ll n$. Such a

problem generally has infinitely many solutions, yet our goal is to robustly recover the particular solution corresponding to the true injected input vector p.

To address this issue, our reconstruction framework leverages the typical sparsity of natural stimuli to utilize compressive sensing theory. Natural scenes and sounds are both sparse in frequency-based domains and odors are sparse in the sense that they are generally composed of a small number of molecule types [52, 114, 83, 123, 64]. For band-limited signals that are sparse in at least a single domain, CS theory demonstrates that, in the sparse domain, the number of nonzero components, rather than the full signal bandwidth [100], determines the minimum sampling rate needed for an accurate reconstruction [35, 46]. In the case of natural scenes, p is typically not sparse in the original spatial domain but $\hat{p} = Tp$ is indeed sparse after applying a sparsifying transform T, such as the discrete cosine or Fourier transform [63, 47]. Upon recovering $\hat{p}$, the sparsifying transform is then inverted to yield p in the original domain.

Since the sparsest solution to Eq. (4.1) well reconciles a small number of samples, a natural way to select $\hat{p}$ is to seek the solution with the smallest number of nonzero components in the sparse domain. However, this approach is typically not possible to implement in polynomial time, and therefore a more efficient method is desirable [29]. For sufficiently sparse $\hat{p}$ and a broad class of measurement matrices, CS theory shows that a viable alternative is minimizing $|\hat{p}|_{\ell_1} = \sum_{i=1}^{n} |\hat{p}_i|$ subject to Eq. (4.1) [36]. This ℓ_1 optimization problem can be efficiently solved in polynomial time using numerous numerical methods [112, 47].

Measurement matrices suitable for CS are generally simple to generate, with a large class of matrices with sufficient randomness, such as those with independent, identically distributed random elements, are proven to satisfy sufficient conditions for accurate recovery [7]. We note that our feedforward connectivity matrix F well satisfies these conditions, and we show in Sect. 7 that even when spatial localization, akin to spatial receptive field structure, is incorporated, CS reconstructions are still highly accurate and in fact often improved.

To reconstruct a gray-scale image input with vectorization $p = (p_1, \dots, p_n)$, we use the two-dimensional discrete cosine transform (2D-DCT) to sparsify the image. We note that for one-dimensional stimuli, such as sound waves, we need only consider a one dimensional transform, and for signal representations of stimuli, such as odorants, that are sparse in their sampled domain, no transforms are necessary.

The $\sqrt{n} \times \sqrt{n}$ 1D-DCT matrix, D, is defined to have entries $D_{ij} = (D^{-1})^T_{ij} = \omega(i) \cos\left(\frac{(i-1)(2j-1)\pi}{2\sqrt{n}}\right)$, where $\omega(1) = (1/n)^{1/4}$ and $\omega(i) = (4/n)^{1/4}$ for $i \neq 1$. The 2D-DCT of an image with vectorization p is $(D \otimes D)p$, where $\otimes$ denotes the $n \times n$ Kronecker product defined such that

$$D \otimes D = \begin{bmatrix} D_{11}D & \cdots & D_{1\sqrt{n}}D \\ \vdots & \ddots & \vdots \\ D_{\sqrt{n}1}D & \cdots & D_{\sqrt{n}\sqrt{n}}D \end{bmatrix}.$$

Given a vectorized input image, to recover the vectorization of its 2D-DCT, $\hat{p}$, we rewrite Eq. (4.1) with respect to the 2D-DCT as

$$\sum_{j=1}^{n} F_{ij}(D \otimes D)^{-1}_{ij} \hat{p}_j = \frac{1}{\alpha} \odot \mu - \frac{1}{\alpha} \odot \beta. \tag{4.2}$$

Considering $\hat{p}$ is sparse, upon measuring the evoked neuronal firing rates, μ, we determine the solution to Eq. (4.2) that minimizes $\sum_{j=1}^{n} |\hat{p}_j|$ to obtain $\hat{p}$ [35, 46]. To finally reconstruct the stimulus in the spatial domain, p, we invert the 2D-DCT and the vectorization.

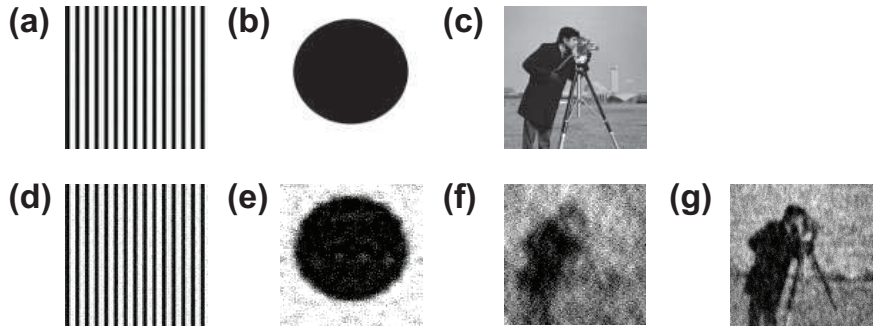


FIG. 2. *(a)-(c): Gray-scale input image stimuli composed of* 100×100 *pixels. (d)-(f): Corresponding CS reconstructions of images in (a)-(c), respectively, using Eq. (4.2) and the data-driven network input-output mapping. The relative reconstruction errors for (d)-(f) are* $0.0624, 0.2201$, *and* 0.3092*, respectively. (g) Reconstruction of the* 250×250 *pixel version of image (c) with relative reconstruction error* 0.2588*. Each CS reconstruction in (d)-(g) uses a factor of* 10 *less downstream I&F neurons than input pixels with current-based neuronal dynamics prescribed by Eq. (2.1).*

Several representative gray-scale image reconstructions using this CS recovery framework in conjunction with the data-driven network input-output mapping are depicted in Fig. 2. To quantify the accuracy of each stimulus reconstruction, p^{recon}, we measure the relative reconstruction error, $\|p - p^{\text{recon}}\|/\|p\|$, using the Euclidean norm, $\|p\| = \sqrt{\sum_i p_i^2}$. We view this error as a measure of information loss along the compressive layer, though the resultant reconstruction may alternatively be interpreted as the stimulus information encoded by the subsequent expansive downstream layer following compression.

For the simpler images in Fig. 2 (a)-(b), we see that the reconstruction is highly accurate even when there are 10 times as many input pixels as downstream neurons, akin to a compressive sensory pathway. For the more complicated cameraman image in Fig. 2 (c), higher error is incurred, but the large-scale features are still well captured and the reconstruction is recognizable. We use this more detailed natural scene as our test stimulus in the subsequent analyses, focusing primarily on 100×100 pixel inputs for computational tractability. The reconstructions obtained using the data-driven input-output mapping, given by Eq. (3.3), are comparable to those analogously obtained via the theoretical mapping, given by Eq. (3.1), but since such theoretical mappings are not feasible to derive for the more detailed models discussed in the following sections, the data-driven approach developed in this work is a necessity.

It is important to emphasize that for higher resolution images with more pixels and generally more sparsity in the frequency domain, it is possible to reconstruct additional, less dominant, image details using the same ratio of downstream to upstream neurons. In Fig. 2 (g), we consider the cameraman image as in Fig. 2 (c) but instead with 250×250 pixels while preserving the compression factor so that there is still a factor of 10 less downstream neurons (i.e., here $m = 6250$ and $n = 62500$). In this higher resolution case, closer to true sensory system layers with potentially millions of neurons, we indeed observe an improved and quite accurate reconstruction.

While the previous reconstructions used the evoked downstream neuronal firing

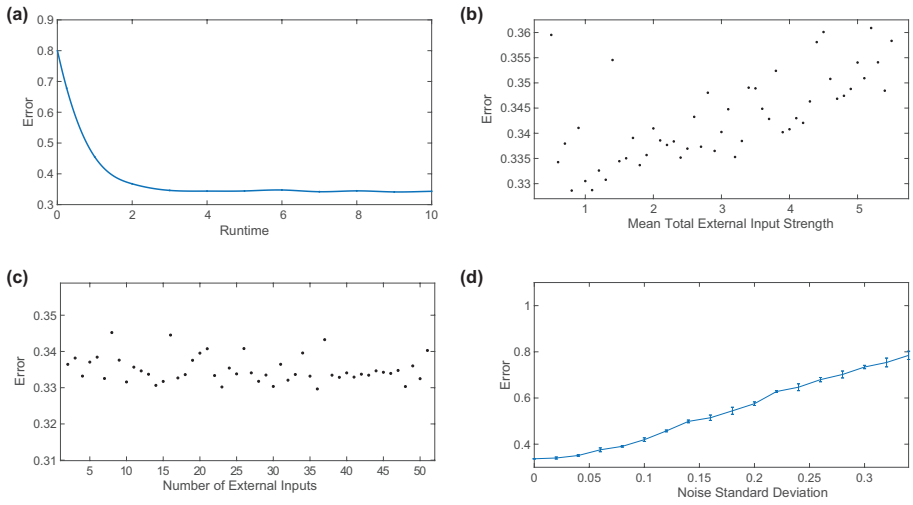


FIG. 3. *(a) Relative reconstruction error as a function of the amount of time over which the network dynamics prescribed by Eq. (2.1) are recorded. (b) Relative reconstruction error as a function of the mean external input strength into the downstream neuronal network. For each data point, the error plotted uses data driven mapping (3.3) fitted with* 11 *different external inputs with strengths centered around the mean strength and strength increments of* 0.1*. (c) Relative reconstruction error as a function of the number of ramped external inputs used to fit Eq. (3.3). For each data point, the mean external input strength is* 2.5 *with strengths equally spaced in* $[1, 4]$ *and centered around the mean. (d) Relative reconstruction error as a function of the standard deviation of the mean* 0 *Gaussian noise multiplying the recorded downstream neuronal firing rates used in the CS reconstruction. The mean relative reconstruction error is plotted over* 5 *realizations with error bars giving the standard deviation in the error across noise realizations. For (a)-(d), each panel considers the CS reconstruction of the image in Fig. 2 (c) utilizing a factor of* 10 *less downstream neurons than pixels and the linear system given by Eq. (4.2).*

rates recorded over $0 \leq t \leq 10$ each, the reconstruction error generally decreases with observation time. In Fig. 3 (a), we depict the relative reconstruction error for the image in Fig. 2 (c) as a function of the simulation runtime, demonstrating a rapid initial decrease in error that later remains nearly constant for sufficiently long simulations, i.e., after approximately $t = 2$ or $40ms$. Hence, the downstream neuronal dynamics in the compressive layer may reliably encode stimulus information over a short and biologically realistic time scale.

With regard to fitting the network input-output mapping, the resultant map is quite insensitive to changes in the number of external inputs used and their strengths. In Fig. 3 (b), we plot the relative reconstruction error using different linear map fittings, where each mapping is obtained using the same number of ramped input vectors but different mean input vector strengths. Here we see that as long as the downstream neuronal dynamics are in the linear regime, the accuracy of the resultant reconstruction is insignificantly impacted by perturbations in the mean input strength used for obtaining the data-driven mapping. Varying the mean input vector strength by a factor of four only results in about 0.02 fluctuations in reconstruction error. Likewise, if we instead hold the mean input vector strength constant in the linear dynamical regime but adjust the number of ramped inputs used, as in Fig. 3 (c), the reconstruction error remains approximately constant so long as at least two input vectors of distinct strengths are used. The ability to successfully reconstruct detailed stimuli using data-driven mappings constructed from a small number of artificial inputs over

a broad range of input strengths underlines both the efficiency and robustness of this methodology.

Reflecting the potential noise in the response of downstream neurons to stimuli, for example due to fluctuations in photon absorption, synaptic release, and neurotransmitter availability [49, 76], we consider how information encoding in this framework is impacted by noise in the downstream neuronal firing rates. To include multiplicative noise, we multiply each downstream neuronal firing rate obtained from simulation by a distinct independent, identically distributed Gaussian random variable with mean 0 and standard deviation σ. We use mean 0 noise based on the assumption that the firing rate fluctuations have no general upward or downward bias. In Figure 3 (d), we plot the relative reconstruction error as a function of the standard deviation σ and observe an approximately linear increase in error with σ. Even when the noise standard deviation is 10% of the firing threshold, the reconstruction error is only increased by about 15%. For each choice of σ, the reconstruction accuracy is nearly constant across multiple noise realizations, highlighting the strong stability of information encoding in neuronal dynamics across compressive pathways.

5. Extensions to Alternative Families of Stimuli.

5.1. Poisson Spike Train Inputs with Image-Based Drive Strengths. To consider alternative forms of compressive pathways, we first adapt our framework to two-layer networks in which feedforward signals are communicated via spike trains rather than graded potentials. In this case, the constant input n-vector is replaced by n Poisson spike trains, reflecting the notion that the time distribution of a large number of spikes received by any given neuron across a large neuronal network is often well approximated by event times generated via a Poisson process [119, 6]. The total mean strengths of the Poisson spike train inputs received by the downstream neurons are determined by the respective components of the constant vector originally injected, namely Fp. In particular, the instantaneous membrane potential jump induced by each feedforward spike from the initial layer is assumed to be held fixed at γ for each downstream neuron and the corresponding rate for the Poisson input is $(Fp)_i/\gamma$ for the i^{th} downstream neuron; this neuron is thus driven by a Poisson spike train with mean drive strength $(Fp)_i$ and its dynamics are determined by Eq. (2.1) aside from the feedforward input modification. Unless specified otherwise, we select the jump strength to be $\gamma = 0.01$.

As shown in Fig. 4 (a), the individual downstream neuronal firing rate responses to Poisson spike train inputs with ramped mean drive strengths are highly linear for sufficiently large drive strengths. In the limit of high incoming Poisson spike train rates and low induced voltage jumps with fixed mean drive strength Fp across the downstream neurons, the drive from the initial layer approaches the original constant input vector [39]. Thus, we use the same methodology as described in Sect. 3 to fit the data-driven input-output mapping across the downstream layer, except now we do this via ramped artificial spike train inputs with their respective mean drive strengths neighboring the slope coefficients in Eq. (3.3). The resultant coefficients in the data-driven network input-output mapping are plotted in Fig. 4 (b), demonstrating nearly the same structure and mean values as in the previous case of constant inputs from the upstream layer. The coefficients in the case of Poisson inputs from the initial layer do display larger variance than in the constant stimulus vector case, but this is to be expected based on randomness introduced by the external spike train input. If instead of using the voltage jump $\gamma = 0.01$, a smaller jump size with higher mean input rate is used, such that the mean drive strength is fixed, the resultant drive

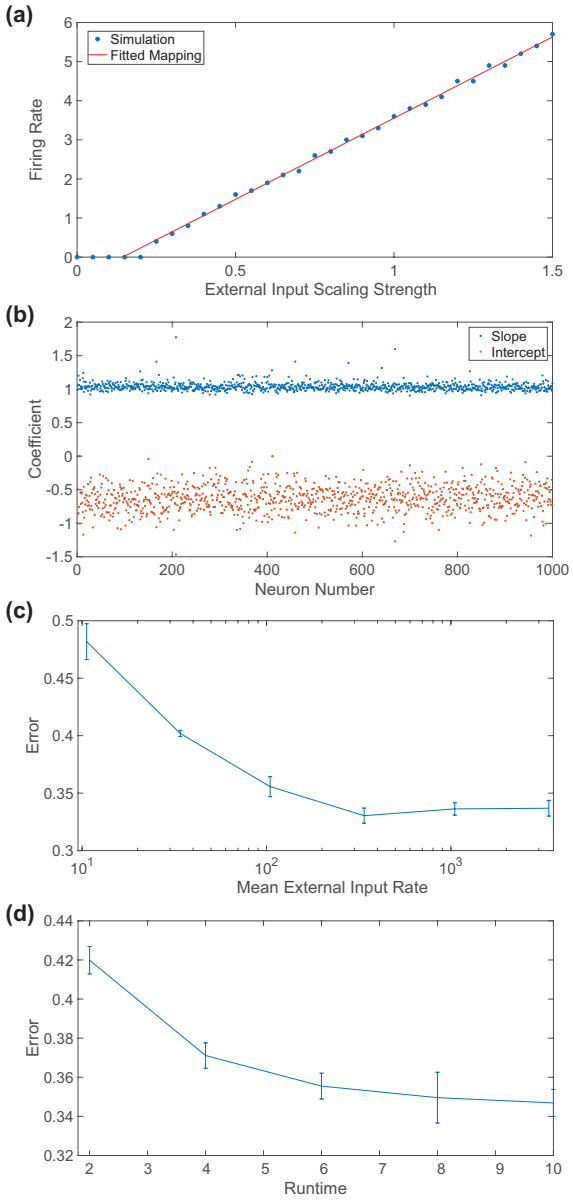


FIG. 4. *(a) Gain curve for an individual downstream neuron in the two-layer network with current-based dynamics and Poisson spike train inputs from the initial layer, depicting the individual neuronal firing rate as a function of the external input strength across several simulations with ramped mean drive strengths. In each case, the voltage jump for the Poisson spike train is fixed at* $\gamma = 0.01$ *and the Poisson input rates are scaled. The input-output mapping for that individual neuron is fitted in the linear regime of the gain curve. (b) Slope and intercept coefficients in Eq. (3.3) fitted for each neuron in (a). (c) Relative reconstruction error dependence on the mean external spike train input rate. The external drive strength for the* i^{th} *downstream neuron is fixed at* $(Fp)_i$ *for* $i = 1, \ldots, m$ *in each case. (d) Relative reconstruction error dependence on the time over which the dynamics described in (a) are recorded. In (c)-(d), the error is plotted over* 5 *realizations of the external input with error bars giving the standard deviation across realizations. CS reconstructions are obtained using the linear system given by Eq. (4.2) and Fig. 2 (c) as input.*

is statistically closer to the original constant input vector considered previously and tighter clustering of the coefficients is achieved.

As long as the rates of the Poisson spike train inputs are sufficiently high, such that each downstream neuron receives a relatively large number of upstream spikes over the observation time, the CS reconstructions obtained using the data-driven mapping display accuracy and stability properties analogous to those discussed for constant inputs. We illustrate this in Fig. 4 (c), where we hold the mean drive strength of the Poisson spike train inputs across the network constant while varying their mean rate and reconstructing the corresponding input stimulus given by Fig. 2 (c) in each case. For each choice of mean Poisson spike train rate, we fit the network input-output mapping over $0 \leq t \leq 10$ and observe little variability in the reconstruction error with accuracy comparable to the constant input case for sufficiently high mean input rates. For lower mean input rates, we note that longer observation times are necessary to well capture the stimulus structure and obtain an accurate reconstruction. As seen in Fig. 4 (d) for a successfully fitted network input-output mapping, the reconstruction error decreases initially with runtime before leveling off when enough downstream neuronal firing events are recorded to well encode the detailed stimulus features.

5.2. Color Image Inputs. To investigate if stimuli with color structure, more representative of natural scenes than gray-scale images, are well encoded along such compressive sensory pathways, we extend our model to RGB (red-green-blue) color image inputs. Here each stimulus in the input layer is represented by three constant n-vectors, corresponding to red, green, and blue intensities, respectively, across all n spatial locations of the pixels. We consider three networks of m downstream I&F neurons, each with unique feedforward and recurrent connectivity matrices, forced by the three respective color intensity vectors.

We fit the network input-output relationship using the downstream neuronal network responses to ramped constant artificial color image inputs with dynamics determined by Eq. (2.1) across each of the three two-layer networks, producing three sets of coefficients for data-driven mapping (3.3). Then, we use the three sets of downstream neuronal firing rate measurements in response to a fixed color image stimulus to reconstruct the corresponding intensity vectors across each of the three color channels via CS and Eq. (4.2). The three intensity vector reconstructions together yield the full color image input reconstruction. Note that since different photoreceptor types respond to different light wavelengths [70] and mammalian visual systems are known to often contain parallel channels [5], we choose to use three distinct compressive pathways to encode color images as opposed to a single pathway with fixed structure.

Several representative color image reconstructions are depicted in Fig. 5. Even in the case of color stimuli with realistic natural scene structure, we observe accurate reconstructions with errors computed across the three channels generally less than those observed in the case of 100×100 pixel gray-scale image inputs. Similar to the reconstructions of higher resolution gray-scale images, the larger number of total pixels across the three color channels facilitates more overall sparsity in the case of color images and thus improved CS reconstructions.

6. Reconstruction Framework for Alternative Network Models.

6.1. Two-Layer Network Model with Conductance-Based Integrate-And-Fire Neuronal Dynamics. While our initial analysis considered the dynamics of the downstream network when determined by current-based I&F neuronal activity, we will now turn to more physiological neuronal models and later more realistic

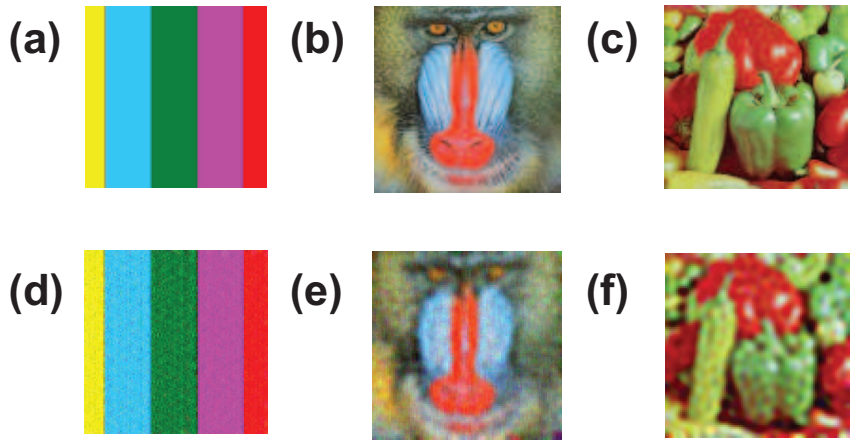


FIG. 5. *(a)-(c): RGB color input image stimuli composed of* 100×100 *pixels for each of the three color intensity vectors (red, green, and blue). (d)-(f): Corresponding CS reconstructions of images in (a)-(c), respectively, using Eq. (4.2) and the network input-output mapping fitted for each color pathway. The relative reconstruction errors for (d)-(f) are* $0.098, 0.134,$ *and* 0.1615*, respectively. Each reconstruction uses a factor of* 10 *less downstream current-based I&F neurons than input pixels in each of the three two-layer networks corresponding to the three different color pathways.*

network coupling. As a first step closer to biological realism, we instead assume that each downstream neuron is governed by conductance-based I&F dynamics. In the conductance-based model, synaptic input currents are now voltage-dependent and produce a richer repertoire of more biophysical dynamics [37, 79]. In particular, the membrane potential of the i^{th} downstream neuron now obeys

$$\frac{dv_i}{dt} = -(v_i - V_R) - \left[\sum_{j=1}^{n} F_{ij} p_j + \frac{S}{N_R} \sum_{\substack{k=1 \\ k\neq i}}^{m} R_{ik} \sum_{l} \delta(t - \tau_{kl})\right](v_i - V_E)\,, \tag{6.1}$$

where $V_E = 14/3$ is the excitatory reversal potential [77] and the remaining terms as well as the network structure are identical to the original two-layer model in Sect. 2.

We now apply our data-driven reconstruction approach to this alternative two-layer network model. First, we fit the input-output mapping (3.3) and then reconstruct constant gray-scale image inputs as outlined in Sect. 4. In Fig. 6 (a), we plot the firing rate of a single downstream neuron in response to ramped artificial constant inputs, similarly demonstrating linear gain for sufficiently strong input scaling strengths, and the resultant network input-output mapping is fit in the broad linear dynamical regime.

In Fig. 6 (b), we depict the corresponding slope and intercept coefficients in mapping (3.3) across the downstream layer. We observe coefficients distinct from those obtained previously, especially in the case of the slopes. Comparing Fig. 1 (b) and Fig. 6 (b), the two linear maps are fairly different, as the slopes and intercepts for the current-based model are clustered near 1 and -0.5, respectively, while those for the conductance-based model are near 4.2 and -0.8. This is to be expected because the analytically derived network input-output mapping in Eq. (3.1) does not apply to neurons with conductance-based dynamics governed by Eq. (6.1). Nevertheless, using

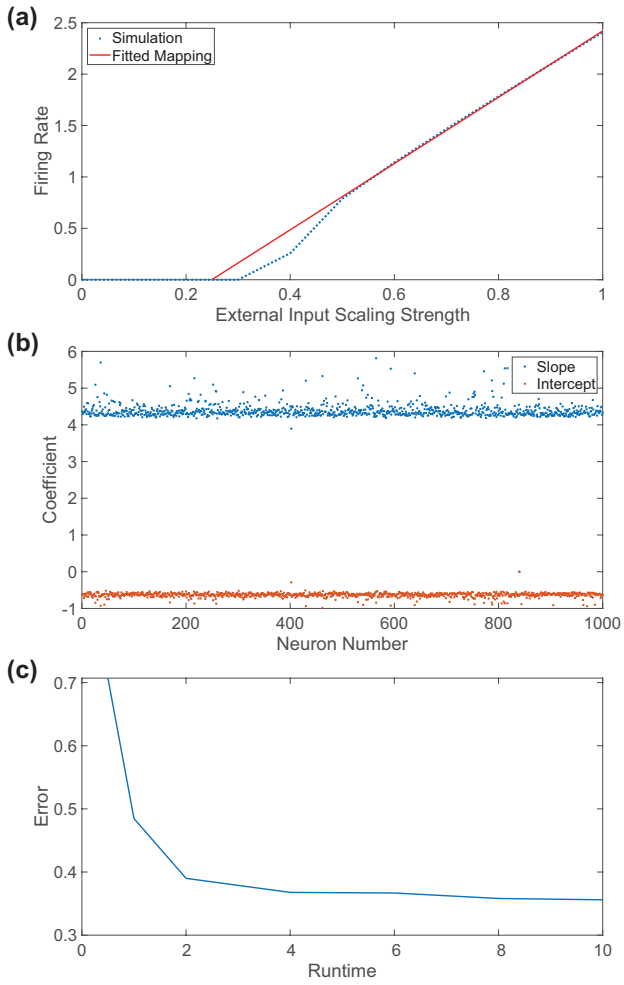


FIG. 6. *(a) Gain curve for an individual downstream neuron in the two-layer network with conductance-based neuronal dynamics prescribed by Eq. (6.1), depicting the individual neuronal firing rate as a function of the external input scaling strength across several simulations with ramped constant external inputs. The input-output mapping for that individual neuron is fitted in the linear regime of the gain curve. (b) Slope and intercept coefficients in Eq. (3.3) fitted for each downstream neuron in the two-layer network considered in (a). (c) Relative reconstruction error as a function of the amount of time over which the network dynamics prescribed by Eq. (6.1) are recorded. Panel (c) considers the CS reconstruction of the image in Fig. 2 (c) utilizing a factor of* 10 *less downstream neurons than pixels and the linear system given by Eq. (4.2).*

CS and the data-driven mapping, we recover input stimuli with accuracy comparable to the reconstructions obtained using the current-based neuronal network model. As shown in Fig. 6 (c), compressive encoding is indeed successful over relatively short time scales when the downstream neurons have conductance-based I&F dynamics.

6.2. Two-Layer Network Model with Conductance-Based Integrate-And-Fire Neuronal Dynamics and Alpha-Function Coupling. Beyond more detailed single neuron dynamics, we investigate the robustness of our compressive encoding framework in the presence of more realistic recurrent neuronal communications

in the downstream layer. Reflecting the brief but finite time course of post-synaptic conductance changes induced by received action potentials, we replace the instantaneous Dirac delta function coupling between downstream neurons with a more physiological α-function time course for the neuronal interactions [101]. In this case, $\delta(t)$ is replaced by

$$g(t) = \frac{t}{\sigma^2} \exp\left(-t/\sigma\right) H(t), \tag{6.2}$$

where $H(t)$ is the Heaviside function, such that $H(t) = 1$ for $t > 0$ and $H(t) = 0$ otherwise, and the finite rise and decay time scales are both controlled by $\sigma = 1/20$ (i.e., $1ms$) [89, 76]. Aside from this change in coupling, we assume the individual downstream neuronal dynamics are conductance-based as in Eq. (6.1).

It is important to emphasize that in the case of this more realistic two-layer model network, analytically deriving an input-output mapping is intractable and thus our data-driven framework provides a more feasible alternative. We observe in Fig. 7 (a) that the individual downstream neuronal firing rate response to sufficiently strong ramped constant external inputs is still linear; thus we apply our methodology to fit a data-driven network input-output mapping prescribed by Eq. (3.3) and obtain the corresponding coefficients plotted in Fig. 7 (b) across the downstream neuronal network. Though the data-driven mapping obtained is distinct from those gleaned for the prior models considered, we achieve similarly accurate input reconstructions for sufficiently long observation times, as displayed in Fig. 7 (c), highlighting the robustness of compressive encoding across sensory pathways with realistic neuronal dynamics. We expect that applying this reconstruction framework for alternative coupling models or different rise and decay time scales will produce comparable results once an appropriate data-driven network input-output mapping is obtained. For these alternative network models, it is also important to note that we are able to well fit the data-driven mapping with a very small number of ramped external inputs over a broad range of mean external input strengths as well as in the presence of noise, just as described for the current-based two-layer network model in Sect. 4.

7. Spatially Localized Random Feedforward Connectivity. In contrast with our previous investigations of encoding across compressive layers in light of increasing biological realism, which focused on the dynamics of individual downstream neurons, their communications, and their external input structure, we conclude by shifting our analysis to the impact of the feedforward connectivity organization. Receptive field structure in feedforward connectivity is shared throughout much of the visual, auditory, somatosensory, and olfactory systems in the sense that downstream neurons are most stimulated by a range of stimuli with similar characteristics [60, 121, 118, 92, 75]. Across sensory system layers, one key consequence of receptive fields is spatial localization in stimulus sampling. In the retina, for example, ganglion cells often exhibit center-surround receptive fields, such that the output of local clusters of photoreceptors is sampled by downstream ganglion cells, exciting ganglion cell activity in on-center locations and inhibiting activity in off-surround locations [120, 66].

To incorporate similar spatial structure into the two-layer network feedforward connectivity, each pixel in the n-component sampled image p is assigned a unique (x, y) location with integer coordinates on a $[1,\ \sqrt{n}] \times [1,\ \sqrt{n}]$ Cartesian grid reflecting all possible pixel locations. Each row of the feedforward connectivity matrix, F, is associated with a distinct random location (x_i, y_i) on this Cartesian grid, around

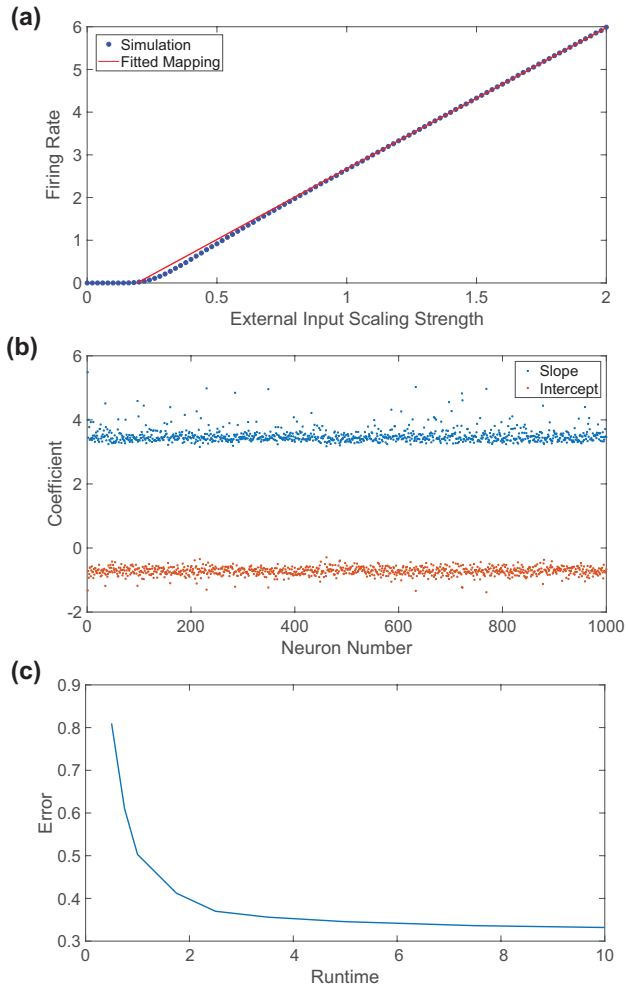


FIG. 7. *(a) Gain curve for an individual downstream neuron in the two-layer network with conductance-based neuronal dynamics prescribed by Eq. (6.1) except with α-function coupling between downstream neurons given by Eq. (6.2), depicting the individual neuronal firing rate as a function of the external input scaling strength across several simulations with ramped constant external inputs. The input-output mapping for that individual neuron is fitted in the linear regime of the gain curve. (b) Slope and intercept coefficients in Eq. (3.3) fitted for each downstream neuron in the two-layer network considered in (a). (c) Relative reconstruction error as a function of the amount of time over which the network dynamics are recorded. Panel (c) considers the CS reconstruction of the image in Fig. 2 (c) utilizing a factor of* 10 *less downstream neurons than pixels and the linear system given by Eq. (4.2).*

which the receptive field of the i^{th} downstream neuron is centered. Reflecting both spatial localization and some degree of randomness in the connectivity, we assume that the probability, P, that the i^{th} downstream neuron samples a pixel with spatial coordinates (x_j, y_j) is given by

$$P = \rho \exp(-[(x_i - x_j)^2 + (y_i - y_j)^2]/[2\sigma^2]), \tag{7.1}$$

where ρ is the sampling probability if $(x_i, y_i) = (x_j, y_j)$, that is when the receptive field center matches the location of a given pixel, and σ characterizes the distance

over which the receptive field samples pixels. Each feedforward connection in a given row i of F can therefore be described by a Bernoulli random variable, determined independently of all other entries of F, with success probability given by Eq. (7.1).

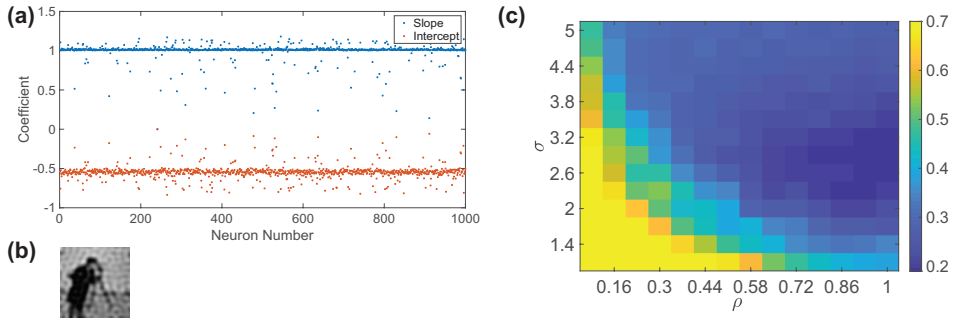


FIG. 8. *(a) Slope and intercept coefficients in Eq. (3.3) fitted for each downstream neuron in the two-layer network with spatially localized random feedforward connectivity prescribed by Eq. (7.1). (b) CS reconstruction of the* 100×100 *pixel image in Fig. 2 (c) using the data-driven linear input-output mapping with coefficients in (a). The sampling probability parameter is* $\rho = 0.9$*, the sampling distance parameter is* $\sigma = 2.5$*, and the relative reconstruction error is* 0.1933*. (c) Relative reconstruction error dependence on the* (ρ, σ) *parameter choice. For each parameter choice, Fig. 2 (c) is reconstructed using a factor of* 10 *less downstream neurons than pixels and current-based neuronal dynamics prescribed by Eq. (2.1).*

Previous work has demonstrated that, relative to the uniformly random feedforward connectivity assumed earlier in this work, sampling analogous to this *spatially localized random feedforward connectivity* more accurately captures the dominant low and moderate frequency components composing an image when using a small number of linear samples [19, 21]. By applying our data-driven reconstruction framework, we examine if this more realistic feedforward connectivity structure is capable of well transmitting stimulus information across the type of compressive pathway modeled initially through the two-layer current-based I&F network discussed in Sect. 2. Even though the feedforward connectivity is now distinct from the uniformly random structure discussed earlier, the slope and intercept coefficients of the resultant network input-output mapping, plotted in Fig. 8 (a), have nearly the same mean values as found previously for downstream neurons with current-based I&F dynamics. Comparing with Fig. 1 (b), relatively uniform clustering about the means is observed in each case, though the variance of the coefficients in the spatially localized case is smaller. This suggests that the network input-output mapping structure is largely determined by the dynamics of the individual downstream neurons and the time course of their communications, which were both shown to impact the fitted coefficients in Sect. 6, whereas the feedforward connectivity structure plays more of a role in determining the stimulus features that are well captured by the downstream network dynamics. The optimal CS reconstruction obtained using spatially localized random feedforward connectivity and the data-driven network input-output mapping for the input stimulus in Fig. 2 (c) is displayed in Fig. 8 (b), exhibiting a reconstruction error approximately half that obtained originally using uniformly random feedforward connectivity.

Since the success of the stimulus encoding in the downstream neuronal dynamics may be intimately tied to the receptive field size and density, we vary feedforward connectivity parameters, ρ and σ, and plot the reconstruction error for each parameter choice in Fig. 8 (c). The optimal σ generates moderately-sized receptive fields and the

corresponding optimal choice of ρ is sufficiently large such that each pixel is expected to be sampled at least once. A local minimum in reconstruction error occurs near $\sigma \approx 2.5$, and even when ρ is as high as $\rho \approx 0.9$, which corresponds to the reconstruction in Fig. 8 (b), the feedforward connectivity matrix is sparse with a connection density of only approximately 0.001. Increasing ρ yet further for fixed σ has little impact on reconstruction quality in this case, and 1 is the upper bound for ρ based on its probabilistic interpretation.

We remark that for simultaneously large ρ and σ, each receptive field collects information from too much of the visual field, resulting in redundancy in the image information obtained by each downstream neuron akin to the uniformly random connectivity considered originally. In this case, a high correlation in the input data received across the downstream network results in diminished reconstruction accuracy. Likewise, for simultaneously small ρ and σ, each receptive field may gather insufficient information across pixel locations and the input into the downstream neurons may be too small to drive the firing events necessary to encode stimulus information, generating extremely large reconstruction error. Overall, for moderately sized receptive fields with relatively sparse connectivity, as often observed in vivo, improved CS reconstructions are achieved. This gives further credence to the hypothesis that sensory systems have evolved to exhibit structure optimized for efficient natural stimulus encoding across compressive pathways.

8. Discussion and Conclusions. We have developed a potential mechanism for the preservation of stimulus information across the ubiquitous compressive pathways in the brain, demonstrating its suitability in the context of numerous two-layer network models with varying degrees of biological realism in both the dynamics of individual neurons and their coupling. Our novel framework for reconstructing input layer information from the nonlinear neuronal activity of a compressive downstream layer was completely driven by simulation data and did not require knowledge of the dynamical system governing the model activity. We approximated a network input-output mapping based on the linear firing rate response of the downstream neurons to a small number of ramped artificial inputs, which is a feature shared by all models investigated in this work for sufficiently strong external input strengths. In conjunction with compressive sensing reconstruction techniques, we used this data-driven network input-output relationship to reconstruct realistic input stimuli taking the form of gray-scale natural scenes, color images, and image-driven Poisson spike trains. By incorporating characteristics of spatial receptive fields into the feedforward connectivity, we also showed that the encoding properties of the downstream neuronal network dynamics are in fact improved, as expected by the prevalence of receptive fields across sensory systems.

This work provides a new proof of concept supporting the notion that such compressive pathways, if designed intelligently, well preserve stimulus information with great efficiency. By containing significantly less neurons in the first downstream layer, stimuli may be rapidly processed in ways that improve encoding capability in the subsequent expansive downstream layers with minimal energy expenditure required [67, 115, 104, 98, 13, 23, 48]. Such processing in the compressive layer may help to reduce redundancy and enhance the function of sensory pathways in performing commonly encountered tasks, such as classification [71, 41].

While our two-layer model was meant to capture the primary shared features of compressive pathways and their mechanisms for stimulus encoding, it would be informative to extend our analysis to models with more detailed physiological struc-

ture corresponding to a specific early sensory system pathway. Such an investigation would benefit from incorporating yet more detailed neuronal activity. We emphasize that even in these more realistic model settings, the linear gain in neuronal response leveraged in our analysis is commonly observed [30, 54, 15, 117], and thus we expect our framework to be naturally extended to such models where analytical techniques, such as coarse-graining, become intractable. Even for highly nonlinear single neuron models, such as the Hodgkin-Huxley model, previous work has successfully produced approximately linear gain curves in the presence of various additional realistic ion channels with dynamics over a range of time scales [74, 25], and the presence of negative feedback in the form of biophysical adaptation currents is known to linearize gain curves that are nonlinear when unadapted [51].

Though our analysis focused on the activity of a downstream layer of excitatory neurons that were largely mean-driven, networks containing additional inhibitory neurons in alternative dynamical regimes, such as the balanced operating state [14, 116, 113], also demonstrate a highly sensitive and linear increase in neuronal activity with external input strength. In general, the neuronal gain curve has been shown to adapt to different stimulus conditions, such as light level in the context of the visual system [27], and potential improvements in stimulus encoding along compressive pathways leveraging this adaptation would mark an interesting area of future investigation. Since our methodology specifically considers dynamical regimes exhibiting linear firing rate gain, it is worth noting that the single neuron models we had analyzed and neurons in experiment nonetheless demonstrate nonlinear voltage dynamics, which are important in their own right and have been shown to enhance feature selectivity [58] as well as decorrelate neuronal responses to stimuli [95, 73].

By more closely mimicking the structure of compressive feedforward pathways, yet further improvements in encoding may be possible using our reconstruction methodology. The size of receptive fields varies widely within a sensory pathway and depending on the receptive field size, details of various scales are measured [99, 45], akin to adjusting the σ parameter in our model of feedforward connectivity with spatially localized structure. By incorporating a diversity of receptive field sizes, we hypothesize that lower amplitude frequency component contributions may be successfully captured with the same number of downstream neurons. Including center-surround antagonism in the feedforward connectivity, which could be modeled using a difference of Gaussians [122, 50], may facilitate the encoding of finer edge information in the downstream neuronal dynamics. Reflecting the architecture of the primary visual cortex by including simple cells in further downstream layers [65, 93], modeled via Gabor functions [42, 85, 72], could also result in orientation selectivity. It would be natural to investigate if additional receptive field types as well as multiple compressive and expansive layers would further improve the encoding of higher order stimulus features. Including these physiological details in the engineering of prosthetic sensory devices and adapting our reconstruction framework to send realistic signals across artificial compressive pathways presents a potential approach to better mitigating sensory impairments [78, 24].

Since in vivo neuronal recordings have been shown to exhibit a linear increase in response with scaled external inputs in certain dynamical regimes [117, 96, 81, 61], our developed framework is likely generalizable to experimental settings seeking to approximate neuronal input-output mappings by making use of intracellular and multielectrode array recordings in response to ramped optogenetic forcing [97, 94]. Once the network input-output relationship is obtained across a pathway of interest, similar CS techniques may be leveraged in order to recover sparse and large-scale neuronal

network connectivity [20, 106, 125, 12]. Since directly measuring structural neuronal connectivity is infeasible for large networks due to, for example, limitations on the spatial resolution of measurement technology [107, 59, 53], such efficient connectivity reconstructions based on recordings of neuronal dynamics are especially valuable in characterizing the structure-function relationship of networks in the brain.

Appendix A. Derivation of the Theoretical Input-Output Mapping for the Current-Based Integrate-And-Fire Neuronal Network.

In deriving the theoretical input-output mapping given by Eq. (3.1), we leverage a coarse-graining approach that applies probabilistic arguments to ultimately obtain a static, linear system relating the network input, stimulus vector p, to the network output, namely the vector of individual downstream neuronal firing rates μ. We focus our analysis in this Appendix on the two-layer current-based integrate-and-fire neuronal network given by Eq. (2.1) because it is analytically tractable, and since this argument does not well extend to more detailed modeling frameworks, we instead resort to our newly developed data-driven approach in the remainder of this work.

We start by analyzing a statistical ensemble of almost identical networks that differ only in their initial membrane potentials, $v_i(t = 0)$, and their resultant input currents, for $i = 1, ..., m$. For each realization of the network, the i^{th} downstream neuron is hence driven by a new independent spike train transmitted by its pre-connected neighbors as well as the external input current, $\sum_{j=1}^{n} F_{ij}p_j$. For each realization of the network in the ensemble, the feed-forward and recurrent connectivity matrices, F and R, respectively, remain fixed.

To more tractably characterize the total drive into each downstream neuron, we assume the network exhibits a large number of firing events, of which each only evokes a relatively small voltage jump to post-connected neurons as typical in vivo. This implies high spike frequency, $\mu_i \gg 0$, and small spike magnitude, $S/N_R \approx 0$. The total recurrent network input into each downstream neuron, say the i^{th}, is

$$\frac{S}{N_R}\sum_{\substack{k=1\\k\neq i}}^{m} R_{ik}\sum_{l}\delta(t-\tau_{kl}),$$

and therefore may be approximated by a Poisson spike train [39]. Statistically, the effect of the rapid recurrent network input approaches the mean drive from pre-connected neurons,

$$\frac{S}{N_R}\sum_{\substack{k=1\\k\neq i}}^{m} R_{ik}\mu_k. \tag{A.1}$$

Replacing the rightmost term of Eq. (2.1) by Eq. (A.1), we obtain the voltage at time t for the i^{th} downstream neuron

$$\begin{aligned} v_i(t) =& v_i(t_0)e^{-(t-t_0)} + \left(1-e^{-(t-t_0)}\right) \\ &\times\left(V_R + \sum_{j=1}^{n} F_{ij}p_j + \frac{S}{N_R}\sum_{\substack{k=1\\k\neq i}}^{m} R_{ik}\mu_k\right). \end{aligned} \tag{A.2}$$

Letting $v_i(t_0) = V_R$, the resting voltage, implies a firing event is expected to occur when $v_i(t_0 + 1/\mu_i) = V_T$, where μ_i is the firing rate of the i^{th} downstream neuron. To obtain a static, nonlinear input-output mapping, we divide by $1 - e^{-1/\mu_i}$, yielding

$$\sum_{j=1}^{n} F_{ij} p_j = \frac{V_T - V_R}{1 - e^{-1/\mu_i}} - \frac{S}{N_R} \sum_{\substack{k=1 \\ k \neq i}}^{m} R_{ik} \mu_k. \tag{A.3}$$

To linearize this mapping, we leverage the earlier assumption that the downstream network is in a high-firing-rate dynamical regime. We Taylor expand with respect to the small parameter $1/(\mu_i)$ and up to the leading order $O(1/(\mu_i)^2)$, we obtain

$$\sum_{j=1}^{n} F_{ij} p_j = \mu_i (V_T - V_R) + \frac{(V_T - V_R)}{2} - \frac{S}{N_R} \sum_{\substack{k=1 \\ k \neq i}}^{m} R_{ik} \mu_k. \tag{A.4}$$

Rewriting Eq. (A.4) across the downstream network, for $i = 1, \ldots, m$, yields the static, linear input-output mapping equivalent to Eq. (3.1),

$$Fp = \left(\mu + \frac{e_m}{2}\right)(V_T - V_R) - \frac{S}{N_R} R\mu, \tag{A.5}$$

where e_m denotes an m-vector of ones. To more closely compare with the data-driven mapping given by Eq. (3.3), we isolate μ above and obtain

$$\left(I - \frac{S}{N_R (V_T - V_R)} R\right) \mu = \frac{Fp}{(V_T - V_R)} - \frac{e_m}{2}. \tag{A.6}$$

Expanding in the form of a Neumann series yields

$$\mu \approx \left(I + \frac{S}{N_R (V_T - V_R)} R + \ldots\right) \left(\frac{Fp}{(V_T - V_R)} - \frac{e_m}{2}\right). \tag{A.7}$$

To leading order, we observe that Eq. (A.7) takes a form analogous to the data-driven mapping, where comparing the mappings shows that across the downstream network the fitted coefficients in this case are $\alpha \approx \frac{1}{(V_T - V_R)}$ and $\beta \approx -\frac{1}{2}$. We also see that the correction term in Eq. (A.7) implies that μ is generally modulated by the number of incoming recurrent connections. This is a primary motivation for the inclusion of the N_R term that normalizes the recurrent connectivity matrix by the total number of recurrent connections in the two-layer network model framework, which keeps the total drive across the downstream network approximately constant with changes in the connection density of R.

REFERENCES

[1] L. Abbott, *Lapicque's introduction of the integrate-and-fire model neuron (1907)*, Brain research bulletin, 50 (1999), pp. 303–304.

[2] K. Amano, N. Goda, S. Nishida, Y. Ejima, T. Takeda, and Y. Ohtani, *Estimation of the timing of human visual perception from magnetoencephalography*, J. Neurosci., 26 (2006), pp. 3981–3991.

[3] S. Ando, Y. Yamada, and M. Kokubu, *Reaction time to peripheral visual stimuli during exercise under hypoxia*, J. Appl. Physiol., 108 (2010), pp. 1210–1216.

[4] B. Babadi and H. Sompolinsky, *Sparseness and expansion in sensory representations*, Neuron, 83 (2014), pp. 1213–1226.

[5] T. Baden, P. Berens, K. Franke, M. Roman Roson, M. Bethge, and T. Euler, *The functional diversity of retinal ganglion cells in the mouse*, Nature, 529 (2016), pp. 345–350.

[6] W. Bair, C. Koch, W. Newsome, and K. Britten, *Power spectrum analysis of bursting cells in area MT in the behaving monkey*, J. Neurosci., 14 (1994), pp. 2870–2892.

[7] R. Baraniuk, *Compressive sensing*, IEEE Signal Processing Mag, (2007), pp. 118–120.

[8] H. Barlow, *Redundancy reduction revisited.*, Network, 12 (2001), pp. 241–253.

[9] H. B. Barlow, *The coding of sensory messages*, in Current Problems in Animal Behaviour, W. H. Thorpe and O. L. Zangwill, eds., Cambridge University Press, 1961, pp. 331–360.

[10] H. B. Barlow, *The ferrier lecture, 1980. critical limiting factors in the design of the eye and visual cortex.*, Proc R Soc Lond B Biol Sci, 212 (1981), pp. 1–34.

[11] V. Barranca, G. Kovacic, and D. Zhou, *The role of sparsity in inverse problems for networks with nonlinear dynamics*, (2019), pp. 1291–1311, https://doi.org/10.4310/CMS.2019.v17.n5.a6.

[12] V. Barranca, D. Zhou, and D. Cai, *Compressive sensing reconstruction of feed-forward connectivity in pulse-coupled nonlinear networks*, Phys. Rev. E, 93 (2016), p. 060201, https://doi.org/10.1103/PhysRevE.93.060201.

[13] V. J. Barranca, H. Huang, and G. Kawakita, *Network structure and input integration in competing firing rate models for decision-making*, J Comput Neurosci, 46 (2019), pp. 145–168.

[14] V. J. Barranca, H. Huang, and S. Li, *The impact of spike-frequency adaptation on balanced network dynamics*, Cogn Neurodyn, 13 (2019), pp. 105–120.

[15] V. J. Barranca, D. C. Johnson, J. L. Moyher, J. P. Sauppe, M. S. Shkarayev, G. Kovačič, and D. Cai, *Dynamics of the exponential integrate-and-fire model with slow currents and adaptation*, J. Comput. Neurosci., 37 (2014), pp. 161–180.

[16] V. J. Barranca, G. Kovačič, D. Zhou, and D. Cai, *Network dynamics for optimal compressive-sensing input-signal recovery*, Phys. Rev. E, 90 (2014), p. 042908.

[17] V. J. Barranca, G. Kovačič, D. Zhou, and D. Cai, *Sparsity and compressed coding in sensory systems*, PLoS Comput. Biol., 10 (2014), p. e1003793.

[18] V. J. Barranca, G. Kovačič, D. Zhou, and D. Cai, *Efficient image processing via compressive sensing of integrate-and-fire neuronal network dynamics*, Neurocomputing, 171 (2016), pp. 1313 – 1322, https://doi.org/http://dx.doi.org/10.1016/j.neucom.2015.07.067, http://www.sciencedirect.com/science/article/pii/S0925231215010747.

[19] V. J. Barranca, G. Kovačič, D. Zhou, and D. Cai, *Improved Compressive Sensing of Natural Scenes Using Localized Random Sampling*, Sci. Rep., 6 (2016), p. 31976.

[20] V. J. Barranca and D. Zhou, *Compressive Sensing Inference of Neuronal Network Connectivity in Balanced Neuronal Dynamics*, Front. Neurosci., 13 (2019), p. 1101.

[21] V. J. Barranca and X. G. Zhu, *A computational study of the role of spatial receptive field structure in processing natural and non-natural scenes*, J. Theor. Biol., 454 (2018), pp. 268–277.

[22] A. Blum, *Random projection, margins, kernels, and feature-selection*, in Proceedings of the 2005 International Conference on Subspace, Latent Structure and Feature Selection, SLSFS'05, Berlin, Heidelberg, 2005, Springer-Verlag, p. 52–68.

[23] R. Bogacz, M. Usher, J. Zhang, and J. L. McClelland, *Extending a biologically inspired model of choice: multi-alternatives, nonlinearity and value-based multidimensional choice*, Philos. Trans. R. Soc. Lond., B, Biol. Sci., 362 (2007), pp. 1655–1670.

[24] P. Bonifazi, F. Difato, P. Massobrio, G. L. Breschi, V. Pasquale, T. Levi, M. Goldin, Y. Bornat, M. Tedesco, M. Bisio, S. Kanner, R. Galron, J. Tessadori, S. Taverna, and M. Chiappalone, *In vitro large-scale experimental and theoretical studies for the realization of bi-directional brain-prostheses*, Front. Neural Circuits, 7 (2013), p. 40.

[25] A. Borisyuk and J. Rinzel, *Understanding neuronal dynamics by geometrical dissection of minimal models*, Methods and Models in Neurophysics (1st Ed., Elsevier, 2005), (2005), pp. 17–72.

[26] M. Brecht and B. Sakmann, *Dynamic representation of whisker deflection by synaptic potentials in spiny stellate and pyramidal cells in the barrels and septa of layer 4 rat somatosensory cortex*, J. Physiol., 543 (2002), pp. 49–70.

[27] N. Brenner, W. Bialek, and R. de Ruyter van Steveninck, *Adaptive rescaling maximizes information transmission*, Neuron, 26 (2000), pp. 695–702.

[28] R. Brette, M. Rudolph, T. Carnevale, M. Hines, D. Beeman, J. M. Bower, M. Diesmann, A. Morrison, P. H. Goodman, F. C. Harris Jr, M. Zirpe, T. Natschlager, D. Pecevski, B. Ermentrout, M. Djurfeldt, A. Lansner, O. Rochel, T. Vieville, E. Muller, A. P. Davison, S. E. Boustani, and A. Destexhe, *Simulation of networks*

of spiking neurons: A review of tools and strategies, J. Comput. Neurosci., 23 (2007), pp. 349–398.

[29] A. Bruckstein, D. Donoho, and M. Elad, *From sparse solutions of systems of equations to sparse modeling of signals and images*, SIAM Review, 51 (2009), pp. 34–81.

[30] N. Brunel and P. Latham, *Firing rate of the noisy quadratic integrate-and-fire neuron*, Neural Comp., 15 (2003), pp. 2281–2306.

[31] A. Burkitt, *A review of the integrate-and-fire neuron model: I. homogeneous synaptic input.*, Biol. Cybern., 95 (2006), pp. 1–19, https://doi.org/10.1007/s00422-006-0068-6.

[32] D. Cai, A. Rangan, and D. McLaughlin, *Architectural and synaptic mechanisms underlying coherent spontaneous activity in V1*, Proc. Nat'l Acad. Sci (USA), 102 (2005), pp. 5868–5873.

[33] D. Cai, L. Tao, A. V. Rangan, and D. W. McLaughlin, *Kinetic theory for neuronal network dynamics*, Commun. Math. Sci., 4 (2006), pp. 97–127.

[34] D. Cai, L. Tao, M. Shelley, and D. McLaughlin, *An effective representation of fluctuation-driven neuronal networks with application to simple & complex cells in visual cortex*, Pro. Nat. Acad. Sci., 101 (2004), pp. 7757–7762.

[35] E. Candes, J. Romberg, and T. Tao, *Stable signal recovery from incomplete and inaccurate measurements*, Commun. Pur. Appl. Math., 59 (2006), pp. 1207–1223.

[36] E. J. Candes and M. B. Wakin, *An Introduction To Compressive Sampling*, Signal Process. Mag., IEEE, 25 (2008), pp. 21–30.

[37] S. Cavallari, S. Panzeri, and A. Mazzoni, *Comparison of the dynamics of neural interactions between current-based and conductance-based integrate-and-fire recurrent networks*, Front. Neural. Circuits, 8 (2014), p. 12.

[38] G. B. Choi, D. D. Stettler, B. R. Kallman, S. T. Bhaskar, A. Fleischmann, and R. Axel, *Driving opposing behaviors with ensembles of piriform neurons*, Cell, 146 (2011), pp. 1004–1015.

[39] E. Cinlar, *Superposition of point processes*, in Stochastic Point Processes: Statistical Analysis, Theory, and Applications, P. Lewis, ed., Wiley, New York, NY, 1972, pp. 549–606.

[40] W. K. Coulter, C. J. Hillar, G. Isley, and F. T. Sommer, *Adaptive compressed sensing - a new class of self-organizing coding models for neuroscience*, in ICASSP, IEEE, 2010, pp. 5494–5497.

[41] S. Dasgupta, C. F. Stevens, and S. Navlakha, *A neural algorithm for a fundamental computing problem*, Science, 358 (2017), pp. 793–796.

[42] J. G. Daugman, *Two-dimensional spectral analysis of cortical receptive field profiles*, Vision Res., 20 (1980), pp. 847–856.

[43] P. Dayan and L. Abbott, *Theoretical Neuroscience*, MIT press, Cambridge, MA, 2001.

[44] D. J. DeBoer and D. I. Vaney, *Gap-junction communication between subtypes of direction-selective ganglion cells in the developing retina*, J. Comp. Neurol., 482 (2005), pp. 85–93.

[45] R. Desimone, T. D. Albright, C. G. Gross, and C. Bruce, *Stimulus-selective properties of inferior temporal neurons in the macaque*, J. Neurosci., 4 (1984), pp. 2051–2062.

[46] D. Donoho, *Compressed sensing*, IEEE Trans. Inform. Theory, 52 (2006), pp. 1289–1306.

[47] D. Donoho and Y. Tsaig, *Fast solution of l_1-norm minimization problems when the solution may be sparse*, IEEE Trans. Inform. Theory, 54 (2008), pp. 4789–4812.

[48] R. J. Douglas and K. A. Martin, *Recurrent neuronal circuits in the neocortex*, Curr. Biol., 17 (2007), pp. 496–500.

[49] F. A. Dunn and F. Rieke, *The impact of photoreceptor noise on retinal gain controls*, Curr. Opin. Neurobiol., 16 (2006), pp. 363–370.

[50] J. H. Elder and A. J. Sachs, *Psychophysical receptive fields of edge detection mechanisms*, Vision Res., 44 (2004), pp. 795–813.

[51] B. Ermentrout, *Linearization of fi curves by adaptation*, Neural computation, 10 (1998), pp. 1721–1729.

[52] D. Field, *What is the goal of sensory coding?*, Neural Computation, 6 (1994), pp. 559–601, https://doi.org/10.1162/neco.1994.6.4.559.

[53] G. D. Field, J. L. Gauthier, A. Sher, M. Greschner, T. A. Machado, L. H. Jepson, J. Shlens, D. E. Gunning, K. Mathieson, W. Dabrowski, L. Paninski, A. M. Litke, and E. J. Chichilnisky, *Functional connectivity in the retina at the resolution of photoreceptors*, Nature, 467 (2010), pp. 673–677.

[54] N. Fourcaud-Trocme and N. Brunel, *Dynamics of the instantaneous firing rate in response to changes in input statistics*, J Comput Neurosci, 18 (2005), pp. 311–321.

[55] S. Ganguli and H. Sompolinsky, *Short-term memory in neuronal networks through dynamical compressed sensing*, in NIPS, Curran Associates, Inc., 2010, pp. 667–675.

[56] S. Ganguli and H. Sompolinsky, *Compressed sensing, sparsity, and dimensionality in neu-*

ronal information processing and data analysis, Annu. Rev. Neurosci., 35 (2012), pp. 485–508.

[57] E. Ganmor, R. Segev, and E. Schneidman, *The architecture of functional interaction networks in the retina*, J. Neurosci., 31 (2011), pp. 3044–3054.

[58] T. Gollisch, *Features and functions of nonlinear spatial integration by retinal ganglion cells*, J. Physiol. Paris, 107 (2013), pp. 338–348.

[59] M. Gomez-Rodriguez, J. Leskovec, and A. Krause, *Inferring networks of diffusion and influence.*, T. Knowl. Discov. D., 5 (2012), p. 21, https://doi.org/10.1145/2086737.2086741.

[60] M. S. Graziano and C. G. Gross, *A bimodal map of space: somatosensory receptive fields in the macaque putamen with corresponding visual receptive fields*, Exp Brain Res, 97 (1993), pp. 96–109.

[61] W. N. Grimes, G. W. Schwartz, and F. Rieke, *The synaptic and circuit mechanisms underlying a change in spatial encoding in the retina*, Neuron, 82 (2014), pp. 460–473.

[62] Y. He, Z. J. Chen, and A. C. Evans, *Small-world anatomical networks in the human brain revealed by cortical thickness from MRI*, Cereb. Cortex, 17 (2007), pp. 2407–2419.

[63] C. Heil and D. Walnut, *Continuous and discrete wavelet transforms*, SIAM review, 31 (1989), pp. 628–666.

[64] T. Hromadka, M. R. Deweese, and A. M. Zador, *Sparse representation of sounds in the unanesthetized auditory cortex*, PLoS Biol., 6 (2008), p. e16.

[65] D. H. Hubel and T. N. Wiesel, *Receptive fields of single neurones in the cat's striate cortex.*, J Physiol, 148 (1959), pp. 574–591.

[66] D. H. Hubel and T. N. Wiesel, *Receptive fields of optic nerve fibres in the spider monkey.*, J Physiol, 154 (1960), pp. 572–580.

[67] M. Humphries, K. Gurney, and T. Prescott, *The brainstem reticular formation is a small-world, not scale-free, network.*, Proc. Biol. Sci., 273 (2006), pp. 503–511, https://doi.org/10.1098/rspb.2005.3354.

[68] G. Isley, C. J. Hillar, and F. T. Sommer, *Deciphering subsampled data: adaptive compressive sampling as a principle of brain communication*, in NIPS, Curran Associates, Inc., 2010, pp. 910–918.

[69] E. M. Izhikevich, *Which model to use for cortical spiking neurons?*, IEEE Trans. Neural. Netw., 15 (2004), pp. 1063–1070.

[70] G. H. Jacobs, *Primate photopigments and primate color vision*, Proc. Natl. Acad. Sci. USA, 93 (1996), pp. 577–581.

[71] J. M. Jeanne and R. I. Wilson, *Convergence, Divergence, and Reconvergence in a Feedforward Network Improves Neural Speed and Accuracy*, Neuron, 88 (2015), pp. 1014–1026.

[72] J. P. Jones and L. A. Palmer, *An evaluation of the two-dimensional Gabor filter model of simple receptive fields in cat striate cortex*, J. Neurophysiol., 58 (1987), pp. 1233–1258.

[73] D. B. Kastner, S. A. Baccus, and T. O. Sharpee, *Critical and maximally informative encoding between neural populations in the retina*, Proc. Natl. Acad. Sci. USA, 112 (2015), pp. 2533–2538.

[74] T. J. Kispersky, J. S. Caplan, and E. Marder, *Increase in sodium conductance decreases firing rate and gain in model neurons*, Journal of Neuroscience, 32 (2012), pp. 10995–11004.

[75] E. I. Knudsen and M. Konishi, *Center-surround organization of auditory receptive fields in the owl*, Science, 202 (1978), pp. 778–780.

[76] C. Koch, *Biophysics of Computation*, Oxford University Press, Oxford, 1999.

[77] G. Kovačič, L. Tao, A. V. Rangan, and D. Cai, *Fokker-planck description of conductance-based integrate-and-fire neuronal networks*, Phys. Rev. E, 80 (2009), p. 021904.

[78] K. Krug, C. D. Salzman, and S. Waddell, *Understanding the brain by controlling neural activity*, Philos. Trans. R. Soc. Lond. B Biol. Sci., 370 (2015), p. 20140201.

[79] A. Kuhn, A. Aertsen, and S. Rotter, *Neuronal integration of synaptic input in the fluctuation-driven regime*, . Neurosci., 24 (2004), pp. 2345–2356.

[80] R. J. Kulesza, A. Vinuela, E. Saldana, and A. S. Berrebi, *Unbiased stereological estimates of neuron number in subcortical auditory nuclei of the rat*, Hear. Res., 168 (2002), pp. 12–24.

[81] G. La Camera, A. Rauch, D. Thurbon, H. R. Luscher, W. Senn, and S. Fusi, *Multiple time scales of temporal response in pyramidal and fast spiking cortical neurons*, J. Neurophysiol., 96 (2006), pp. 3448–3464.

[82] Y. LeCun, Y. Bengio, and G. Hinton, *Deep learning*, Nature, 521 (2015), pp. 436–444.

[83] A. C. Lin, A. M. Bygrave, A. de Calignon, T. Lee, and G. Miesenbock, *Sparse, decorrelated odor coding in the mushroom body enhances learned odor discrimination*, Nat. Neurosci., 17 (2014), pp. 559–568.

952 [84] S. X. Luo, R. Axel, and L. F. Abbott, *Generating sparse and selective third-order responses*
953 *in the olfactory system of the fly*, Proc. Natl. Acad. Sci. USA, 107 (2010), pp. 10713–
954 10718.
955 [85] S. Marcelja, *Mathematical description of the responses of simple cortical cells*, J Opt Soc
956 Am, 70 (1980), pp. 1297–1300.
957 [86] A. Maresh, D. Rodriguez Gil, M. C. Whitman, and C. A. Greer, *Principles of glomerular*
958 *organization in the human olfactory bulb–implications for odor processing*, PLoS One, 3
959 (2008), p. e2640.
960 [87] H. Markram, J. Lubke, M. Frotscher, A. Roth, and B. Sakmann, *Physiology and*
961 *anatomy of synaptic connections between thick tufted pyramidal neurones in the devel-*
962 *oping rat neocortex.*, J. Physiol., 500 (Pt 2) (1997), pp. 409–440.
963 [88] W. Mather, M. R. Bennett, J. Hasty, and L. S. Tsimring, *Delay-induced degrade-and-fire*
964 *oscillations in small genetic circuits*, Phys. Rev. Lett., 102 (2009), p. 068105.
965 [89] D. McLaughlin, R. Shapley, M. Shelley, and D. J. Wielaard, *A neuronal network model*
966 *of macaque primary visual cortex (v1): Orientation selectivity and dynamics in the input*
967 *layer 4cα*, Proceedings of the National Academy of Sciences, 97 (2000), pp. 8087–8092,
968 https://doi.org/10.1073/pnas.110135097.
969 [90] D. McLaughlin, R. Shapley, M. Shelley, and J. Wielaard, *A neuronal network model of*
970 *macaque primary visual cortex (V1): Orientation selectivity and dynamics in the input*
971 *layer 4Cα*, Proc. Natl. Acad. Sci. USA, 97 (2000), pp. 8087–8092.
972 [91] R. E. Mirollo and S. H. Strogatz, *Synchronization of pulse-coupled biological oscillators*,
973 SIAM Journal on Applied Mathematics, 50 (1990), pp. 1645–1662.
974 [92] K. Mori, H. Nagao, and Y. Yoshihara, *The olfactory bulb: coding and processing of odor*
975 *molecule information*, Science, 286 (1999), pp. 711–715.
976 [93] C. M. Niell, *Cell types, circuits, and receptive fields in the mouse visual cortex*, Annu. Rev.
977 Neurosci., 38 (2015), pp. 413–431.
978 [94] A. M. Packer, L. E. Russell, H. W. Dalgleish, and M. Hausser, *Simultaneous all-optical*
979 *manipulation and recording of neural circuit activity with cellular resolution in vivo*, Nat.
980 Methods, 12 (2015), pp. 140–146.
981 [95] X. Pitkow and M. Meister, *Decorrelation and efficient coding by retinal ganglion cells*, Nat.
982 Neurosci., 15 (2012), pp. 628–635.
983 [96] A. Rauch, G. La Camera, H. Luscher, W. Senn, and S. Fusi, *Neocortical pyramidal cells*
984 *respond as integrate-and-fire neurons to in vivo-like input currents.*, J Neurophysiol, 90
985 (2003), pp. 1598–1612, https://doi.org/10.1152/jn.00293.2003.
986 [97] J. P. Rickgauer, K. Deisseroth, and D. W. Tank, *Simultaneous cellular-resolution optical*
987 *perturbation and imaging of place cell firing fields*, Nat. Neurosci., 17 (2014), pp. 1816–
988 1824.
989 [98] A. Roxin, H. Riecke, and S. Solla, *Self-sustained activity in a small-world network*
990 *of excitable neurons*, Phys. Rev. Lett., 92 (2004), p. 198101, https://doi.org/10.1103/
991 PhysRevLett.92.198101.
992 [99] M. P. Sceniak, D. L. Ringach, M. J. Hawken, and R. Shapley, *Contrast's effect on spatial*
993 *summation by macaque V1 neurons*, Nat. Neurosci., 2 (1999), pp. 733–739.
994 [100] C. E. Shannon, *Communication in the Presence of Noise*, Proceedings of the IRE, 37 (1949),
995 pp. 10–21.
996 [101] D. Somers, S. Nelson, and M. Sur, *An emergent model of orientation selectivity in cat*
997 *visual cortical simple cells*, Journal of Neuroscience, 15 (1995), pp. 5448–5465.
998 [102] D. L. Sosulski, M. L. Bloom, T. Cutforth, R. Axel, and S. Datta, *Dis-*
999 *tinct representations of olfactory information in different cortical centres*, Nature,
1000 472 (2011), p. 213—216, https://doi.org/10.1038/nature09868, https://europepmc.org/
1001 articles/PMC3354569.
1002 [103] P. D. Spear, C. B. Kim, A. Ahmad, and B. W. Tom, *Relationship between numbers of*
1003 *retinal ganglion cells and lateral geniculate neurons in the rhesus monkey*, Vis. Neurosci.,
1004 13 (1996), pp. 199–203.
1005 [104] O. Sporns and C. Honey, *Small worlds inside big brains.*, Proc Natl Acad Sci U S A, 103
1006 (2006), pp. 19219–19220, https://doi.org/10.1073/pnas.0609523103.
1007 [105] P. Sterling and S. Laughlin, *Principles of Neural Design*, 06 2015, https://doi.org/10.
1008 7551/mitpress/9780262028707.001.0001.
1009 [106] O. Stetter, D. Battaglia, J. Soriano, and T. Geisel, *Model-free reconstruction of excita-*
1010 *tory neuronal connectivity from calcium imaging signals*, PLoS Comput. Biol., 8 (2012),
1011 p. e1002653.
1012 [107] I. H. Stevenson, J. M. Rebesco, L. E. Miller, and K. P. Kording, *Inferring functional*
1013 *connections between neurons*, Curr. Opin. Neurobiol., 18 (2008), pp. 582–588.

[108] W. B. Thoreson, *Kinetics of synaptic transmission at ribbon synapses of rods and cones.*, Mol Neurobiol, 36 (2007), pp. 205–223, https://doi.org/10.1007/s12035-007-0019-9.
[109] S. Trenholm, D. J. Schwab, V. Balasubramanian, and G. B. Awatramani, *Lag normalization in an electrically coupled neural network*, Nat. Neurosci., 16 (2013), pp. 154–156, https://doi.org/10.1038/nn.3308.
[110] A. Treves, *Mean field analysis of neuronal spike dynamics*, Network, 4 (1993), pp. 259–284.
[111] P. K. Trong and F. Rieke, *Origin of correlated activity between parasol retinal ganglion cells*, Nat. Neurosci., 11 (2008), pp. 1343–1351.
[112] J. A. Tropp and A. C. Gilbert, *Signal Recovery From Random Measurements Via Orthogonal Matching Pursuit*, IEEE Trans. Inform. Theory, 53 (2007), pp. 4655–4666.
[113] T. W. Troyer and K. D. Miller, *Physiological gain leads to high ISI variability in a simple model of a cortical regular spiking cell*, Neural Comput, 9 (1997), pp. 971–983.
[114] G. C. Turner, M. Bazhenov, and G. Laurent, *Olfactory representations by Drosophila mushroom body neurons*, J. Neurophysiol., 99 (2008), pp. 734–746.
[115] M. van den Heuvel, C. Stam, M. Boersma, and H. Hulshoff Pol, *Small-world and scale-free organization of voxel-based resting-state functional connectivity in the human brain.*, Neuroimage, 43 (2008), pp. 528–539, https://doi.org/10.1016/j.neuroimage.2008.08.010.
[116] C. van Vreeswijk and H. Sompolinsky, *Chaos in neuronal networks with balanced excitatory and inhibitory activity*, Science, 274 (1996), pp. 1724–1726.
[117] X. J. Wang, *Calcium coding and adaptive temporal computation in cortical pyramidal neurons*, J. Neurophysiol., 79 (1998), pp. 1549–1566.
[118] C. Welker, *Receptive fields of barrels in the somatosensory neocortex of the rat*, J. Comp. Neurol., 166 (1976), pp. 173–189.
[119] G. Werner and V. B. Mountcastle, *Neural activity in mechanoreceptive cutaneous afferents: Stimulus-response relations, Weber functions, and information transmission*, J. Neurophysiol., 28 (1965), pp. 359–397.
[120] T. N. Wiesel, *Receptive fields of ganglion cells in the cat's retina*, J Physiol, 153 (1960), pp. 583–594.
[121] D. A. Wilson, *Receptive fields in the rat piriform cortex*, Chem. Senses, 26 (2001), pp. 577–584.
[122] A. Wohrer and P. Kornprobst, *Virtual retina: a biological retina model and simulator, with contrast gain control.*, J Comput Neurosci, 26 (2009), pp. 219–249, https://doi.org/10.1007/s10827-008-0108-4.
[123] C. Yu, K. Prokop-Prigge, L. Warrenburg, and J. Mainland, *Drawing the borders of olfactory space*, in Chemical Senses, vol. 40, OXFORD UNIV PRESS GREAT CLARENDON ST, OXFORD OX2 6DP, ENGLAND, 2015, pp. 565–565.
[124] L. Zhaoping, *A new framework for understanding vision from the perspective of the primary visual cortex*, Curr. Opin. Neurobiol., 58 (2019), pp. 1–10.
[125] D. Zhou, Y. Xiao, Y. Zhang, Z. Xu, and D. Cai, *Causal and structural connectivity of pulse-coupled nonlinear networks*, Phys. Rev. Lett., 111 (2013), p. 054102.